JOURNAL OF APPLIED CRYSTALLOGRAPHY
ISSN 1600-5767

RADDOSE-XFEL: femtosecond time-resolved dose estimates for macromolecular X-ray free-electron laser experiments

Joshua L. Dickerson, Patrick T. N. McCubbin and Elspeth F. Garman*

Department of Biochemistry, University of Oxford, South Parks Road, Oxford OX1 3QU, UK. *Correspondence e-mail: elspeth.garman@bioch.ox.ac.uk

Received 26 August 2019
Accepted 20 January 2020

Edited by J. Hajdu, Uppsala University, Sweden and The European Extreme Light Infrastucture, Czech Republic

Keywords: radiation damage; dose; X-ray free-electron lasers; XFELs; protein crystallography; serial femtosecond crystallography; computer programs.

Supporting information: this article has supporting information at journals.iucr.org/j

For macromolecular structure determination at synchrotron sources, radiation damage remains a major limiting factor. Estimation of the absorbed dose (J kg^{-1}) during data collection at these sources by programs such as *RADDOSE-3D* has allowed direct comparison of radiation damage between experiments carried out with different samples and beam parameters. This has enabled prediction of roughly when radiation damage will manifest so it can potentially be avoided. X-ray free-electron lasers (XFELs), which produce intense X-ray pulses only a few femtoseconds in duration, can be used to generate diffraction patterns before most of the radiation damage processes have occurred and hence hypothetically they enable the determination of damage-free atomic resolution structures. In spite of this, several experimental and theoretical studies have suggested that structures from XFELs are not always free of radiation damage. There are currently no freely available programs designed to calculate the dose absorbed during XFEL data collection. This article presents an extension to *RADDOSE-3D* called *RADDOSE-XFEL*, which calculates the time-resolved dose during XFEL experiments. It is anticipated that *RADDOSE-XFEL* could be used to facilitate the study of radiation damage at XFELs and ultimately be used prior to data collection so that experimenters can plan their experiments to avoid radiation damage manifesting in their structures.

1. Introduction

Since the beginning of X-ray macromolecular crystallography (MX), radiation damage (Blake & Phillips, 1962) has been one of the most common causes of structure determination failure. X-rays deposit energy as they interact with the sample by the Compton effect, where a photon loses some energy to a recoil electron, and by the photoelectric effect, where the photon is absorbed and a photoelectron, usually from the innermost shell of a constituent atom, is released with energy equal to the photon energy minus the electron shell binding energy (Einstein, 1905). The hollow ion relaxes by de-excitation of an electron from a higher shell to fill the vacancy. This is followed by the release of energy in the form of a fluorescent photon (Moseley, 1913) or another electron called an Auger electron (Meitner, 1922; Auger, 1925), with the probability of fluorescent X-ray emission increasing with atomic number (Z) (Krause, 1979).

Energy deposited in the sample by X-rays from these effects causes chemical and physical changes, altering the structure of the crystal. However, most of the damage is caused by photoelectrons emitted after photoelectric absorption. A 12 keV photoelectron can give rise to up to ~500 further

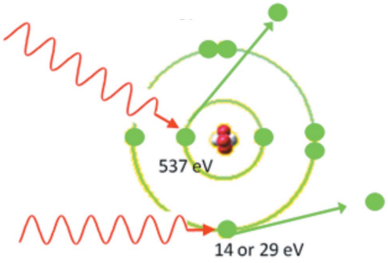

ionization events in the sample, assuming an average energy loss per ionization event of 25 eV (O'Neill *et al.*, 2002).

The effects of radiation damage at synchrotrons can be reduced by cryo-cooling the crystal in liquid nitrogen to 77 K and then collecting data at 100 K in a stream of gaseous nitrogen. This prolongs the crystal lifetime by a factor of ~30–70 (Nave & Garman, 2005; Warkentin & Thorne, 2010) by stopping the movement of most free radicals. However, electrons, holes and hydrogen atoms are still mobile at cryogenic temperatures so radiation damage can still progress.

X-ray free-electron lasers (XFELs) promise high-resolution protein structures that are free from damage. Femtosecond pulses with high brilliance are generated by XFELs and can be used to collect X-ray diffraction patterns from a fully hydrated stream of nanocrystals (Chapman *et al.*, 2011). A monochromator is often used to select a specific X-ray wavelength, although foregoing this to produce a polychromatic beam (pink beam) increases pulse intensity. The intense pulse (which can be $\gg 10^{17}$ W cm^{-2}; Chapman *et al.*, 2014) completely vaporizes the sample by a 'Coulomb explosion', but a diffraction pattern is first obtained, usually before significant radiation damage has occurred. This possibility was first predicted and described in a classic paper by Neutze *et al.* (2000), who performed molecular dynamics simulations using a modified version of *GROMACS* (Berendsen *et al.*, 1995) to investigate the molecular disintegration of both single and 4 × 4 × 4 arrays of T4 lysozyme molecules as a function of the XFEL pulse length. They investigated the effect of different pulse lengths and the 'landscape of radiation tolerance', concluding that, for a 2 fs 12 keV pulse of size 100 nm FWHM which contained 3×10^{12} photons, diffraction would be over before significant displacement of the atoms in the structure could occur. This prediction was later verified experimentally in principle both for single particles of the large (~0.75 µm) mimivirus (Seibert *et al.*, 2011) and for nanocrystals (all <2 µm) of photosystem I (Chapman *et al.*, 2011) using 70 fs XFEL pulses. During the pulse, atomic ionizations occur randomly and modify the scattering amplitudes of atoms. As the degree of atomic displacement increases throughout the pulse, the correlation of structure between unit cells in a crystal sample is lost and the contribution to Bragg peaks reduces, being eventually lost. Plasma dynamics simulations (Barty *et al.*, 2012) using the program *CRETIN* (Scott & Mayle, 1994; Scott, 2001) have demonstrated this for XFEL sources, showing that, after a certain time during a pulse, atomic displacements will be large enough that contributions to the Bragg peaks of a particular resolution shell cease for the remainder of the pulse, and then only additional background is collected.

A further phenomenon is the loss of inner-shell electrons in the constituent atoms, leading to 'hollow atoms' whose X-ray scattering cross sections are lower than those for their native states which results in a degree of 'radiation hardening' and transient X-ray transparency, shown experimentally for neon atoms (Son *et al.*, 2011). This electron loss also causes positive charge build-up and interatomic repulsion. For longer pulse lengths, the kinetic energy of the system exceeds its potential energy and the sample explodes. Single molecules and small clusters are believed to suffer from a Coulomb explosion (Neutze *et al.*, 2000), whereas larger clusters and micrometre-sized crystals are more likely to undergo a hydrodynamic expansion due to electron pressure and heating (Ditmire, 2016).

In practice, pulse lengths are not necessarily short enough (Hau-Riege *et al.*, 2004, 2005), and flux densities (photons per second per area) not necessarily high enough, to obtain a useful signal before any radiation damage occurs. As a result, radiation damage has been observed in XFEL structures (Lomb *et al.*, 2011; Nass *et al.*, 2015; Galli *et al.*, 2015), particularly at heavy-atom sites as would be expected in a synchrotron experiment.

The absorbed dose D, defined as the energy absorbed per unit mass in SI units of gray (Gy = J kg^{-1}), is a generally accepted metric against which to quantify the progression of radiation damage in MX. Dose cannot be measured directly but can be estimated using knowledge of the crystal (size and composition), beam (intensity profile, energy, flux, size) and exposure time.

The program *RADDOSE v1* (Murray *et al.*, 2004) estimated the dose absorbed during MX data collection using the following equation:

$$D \propto \frac{I_0}{\lambda V}\left[1 - \exp(-\mu_{\rm abs} t)\right] \quad \text{with} \quad \mu_{\rm abs} = \frac{1}{V}\sum_{j=1}^{N} \sigma_{\rm pe}, \qquad (1)$$

where I_0 is the incident intensity of the beam, λ is the incident X-ray wavelength, V is the crystal volume, t is the crystal thickness, N is the total number of atoms j and $\mu_{\rm abs}$ is the photoelectric absorption coefficient of the crystal, estimated from the sum of the atomic photoelectric cross sections, $\sigma_{\rm pe}$, of all atoms in the crystal at the relevant incident X-ray wavelength.

Equation (1) used in *RADDOSE v1* only includes the photoelectric effect, which is the dominant interaction at the incident X-ray energies ($E_{\rm inc}$) commonly used in MX (~10–15 keV). *RADDOSE v2* (Paithankar *et al.*, 2009) included the probability of fluorescent photons escaping the crystal and reducing the dose, which is important for high-Z elements. *RADDOSE v3* included energy loss in the crystal due the Compton effect, which becomes significant when $E_{\rm inc}$ > 20 keV. The current version, *RADDOSE-3D* (Zeldin, Gerstel & Garman, 2013; Bury *et al.*, 2018), was created as a result of the beams being used for MX at synchrotrons reducing in size, so that crystals were commonly larger than the beam. *RADDOSE-3D* partitions the crystal into evenly spaced voxels (volume elements) of a user-defined size, as well as dividing the crystal rotation into a discrete number of steps. This allows spatially and temporally resolved dose maps to be calculated as the crystal is irradiated and rotated.

In XFEL experiments, doses are currently calculated using *RADDOSE-3D* or a similar method, and structures have been solved at doses in the GGy range (Chapman *et al.*, 2011; Lomb *et al.*, 2011; Barty *et al.*, 2012), two orders of magnitude higher than the experimental dose limit of 30 MGy proposed for MX

at 100 K (Owen *et al.*, 2006). However, these calculations assume that all the energy from absorbed photons remains within the sample. This is not valid, since photoelectrons can travel far enough to escape microcrystals, which reduces the absorbed dose (Nave & Hill, 2005; Sanishvili *et al.*, 2011; Fourme *et al.*, 2012; Marman *et al.*, 2018; Dickerson & Garman, 2019). Furthermore, the short pulses mean that a diffraction pattern is obtained before the photoelectrons have lost their energy and caused significant damage. A simulation analysis predicted that pulses shorter than 0.1 fs could outrun the first impact of 12 keV photoelectrons (Son *et al.*, 2011). Realistic dose calculations therefore need to track photons and photoelectrons in a time-resolved manner on the femtosecond timescale to determine the absorbed dose at the time of diffraction pattern collection.

Here, we present a new extension to *RADDOSE-3D*, *RADDOSE-XFEL*, which uses Monte Carlo simulations to more realistically estimate the dose absorbed at XFEL sources. We first describe the Monte Carlo simulations used in *RADDOSE-XFEL* before detailing how to use the program. Finally, we discuss the applications of *RADDOSE-XFEL*, as well as its limitations and planned future developments.

2. The *RADDOSE-XFEL* code

For *RADDOSE-XFEL*, the crystal is partitioned into evenly spaced voxels of a user-defined size and the dose in each voxel is tracked from the time the first photon in the pulse enters it until the last photon exits. The same treatment is used both for cases where the crystal is smaller than the beam and where the crystal is larger than the beam. The program divides the crystal up into many voxels and these must be significantly smaller than the beam. Even when the beam is larger than the crystal, a significant number of voxels are required to allow the necessary time resolution. As detailed below, the XFEL photon–matter interactions are described using the following basic physics: X-ray cross sections from the XCOM database (Berger *et al.*, 2010), lifetimes of excited atomic state from the EADL (Evaluated Atomic Data Library) database (Cullen *et al.*, 1991; Cullen, 1992), differential electron outer-shell interaction cross sections calculated through the generalized oscillator strength (GOS) model (Salvat *et al.*, 2001), and inner-shell electron interaction cross sections from a combination of the plane-wave Born approximation (PWBA) and distorted-wave Born approximation (DWBA) (Bote *et al.*, 2009). The overall architecture of the code is shown in Fig. 1.

2.1. Photon simulations

In *RADDOSE-XFEL*, the user defines the number of photons to be simulated and each photon is tracked independently.

A photon is first placed randomly within the user-selected top-hat or Gaussian beam intensity profile, which is collimated either as rectangular or elliptical/circular. The centre of the beam is assumed on average to coincide with the centre of the microcrystal. The initial coordinates of each simulated photon in the exposed area are generated by random inverse transform sampling, with x being the horizontal, y the vertical and z the beam axis. The energy of the photon is then assigned. If a polychromatic beam is used, the distribution of photon energies is currently assumed to be Gaussian, where the mean and FWHM of the distribution can be specified by the user. This assumption attempts to capture most of the effect of having a spread of photon energies, particularly around absorption edges. Each photon being simulated is assigned its energy on the basis of systematic inverse transform sampling of this distribution. If no FWHM is specified, all photons are given the same energy as specified by the user, corresponding to a monochromatic beam.

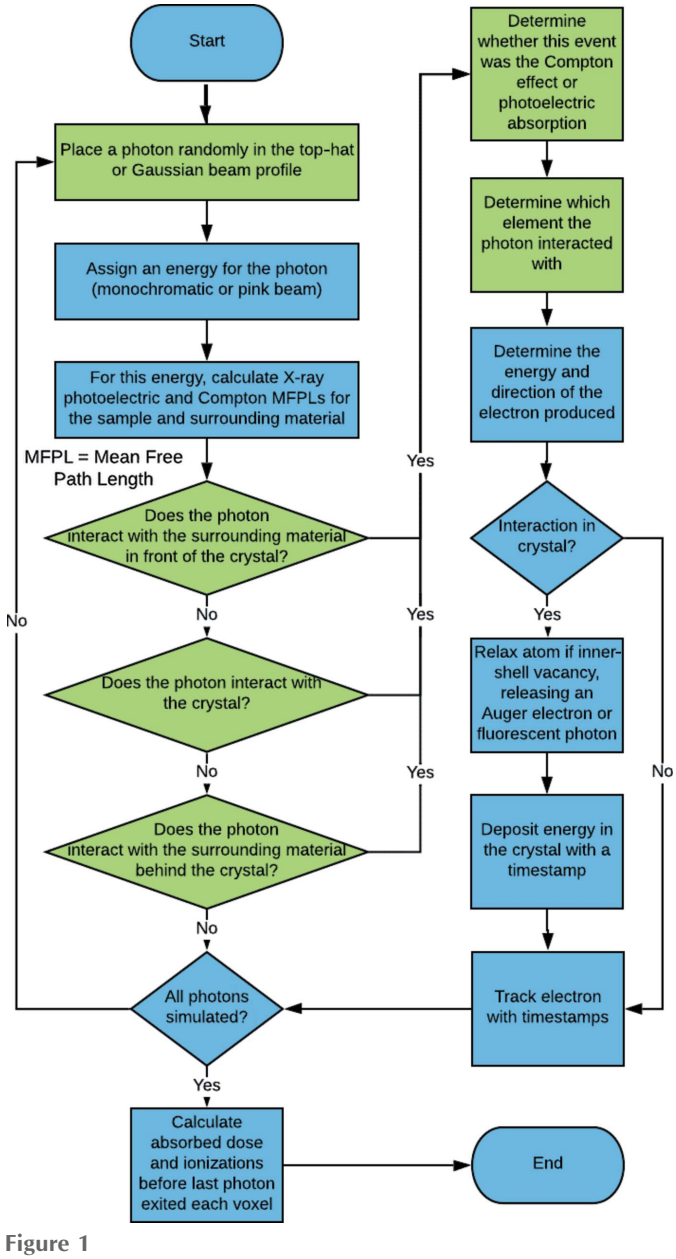

Figure 1
A description of the logical flow of the code in *RADDOSE-XFEL*. For green processes, random numbers were used to sample from probability density functions.

The composition of the crystal and the surrounding material are defined using the same input as for *RADDOSE-3D*. Simulation of the surrounding material allows one to account for photoelectrons or Compton recoil electrons entering from it, as this can alter the absorbed dose depending on the relative sizes of the crystal and the beam. The surroundings will also attenuate photons, although this effect is neglected in *RADDOSE-XFEL* since the photoelectric mean free path length (MFPL) of 10 keV X-rays in pure water is 2.13 mm, so <0.5% of photons are absorbed in a 10 µm thickness. Electrons are only simulated within a distance from the crystal equal to $E_{\rm inc}/S_{\rm col}$, where the collision stopping power $S_{\rm col}$ is calculated according to supplementary material Section 1, with the electron energy being set equal to $E_{\rm inc}$. It is unlikely that electrons produced beyond this distance will reach the sample, and hence they are neglected.

The photoelectric, Compton and total MFPLs to the next ionizing interaction of the photon ($\lambda_{\rm photo}$, $\lambda_{\rm comp}$ and $\lambda_{\rm tot}$, respectively) are then calculated using equation (2) below. The photoelectric and Compton scattering cross sections for each element j ($\sigma_j^{\rm photo}$ and $\sigma_j^{\rm comp}$, respectively) are taken from the XCOM database (Berger *et al.*, 2010):

$$\lambda_{\rm photo} = \left(\sum_j \frac{\sigma_j^{\rm photo} N_j}{V}\right)^{-1},$$
$$\lambda_{\rm comp} = \left(\sum_j \frac{\sigma_j^{\rm comp} N_j}{V}\right)^{-1}, \quad (2)$$
$$\lambda_{\rm tot} = \left(\frac{1}{\lambda_{\rm photo}} + \frac{1}{\lambda_{\rm comp}}\right).$$

The distance to the next interaction, s, is then sampled using equation (3) (Joy, 1995), where RND is a random number between 0 and 1:

$$s = -\lambda_{\rm tot} \ln({\rm RND}). \quad (3)$$

If the photon interacts with the crystal or the surrounding material, the type of interaction (Compton or photoelectric) is determined via random inverse transform sampling using the relative probabilities of each type of event. For a photoelectric absorption event, the element shell from which the photoelectron will originate is calculated via the inverse transform method using the relative absorption probability of each elemental shell. The initial energy of the photoelectron is set to $E_{\rm inc}$ minus the shell binding energy, and the initial timestamp is the time of absorption. The initial direction of the photoelectron is not random but is biased in the beam polarization direction. Synchrotron radiation is horizontally polarized (supplementary material Section 2), and *RADDOSE-XFEL* assumes that XFEL radiation is similar, although users can specify a vertically polarized beam if appropriate (*e.g.* as for the new LCLS hard X-ray undulator which has been rotated by 90°). Circularly polarized XFEL radiation cannot currently be specified in *RADDOSE-XFEL*. Photoelectrons are preferentially emitted in the direction of the polarization vector (supplementary material Section 2). From supplementary material Section 2, equation (5), and using the coordinate system defined above, the angle to the polarization vector is obtained and its cosine provides the X value of the direction vector of the ejected electron. The direction vector Y and Z values are chosen randomly, ensuring that the magnitude of the vector equals 1. *RADDOSE-XFEL* uses a polar coordinate system to track the photoelectrons (and other electrons produced), and the coordinates can be converted using the following relationship:

$$\text{electron direction vector} = \begin{pmatrix} X \\ Y \\ Z \end{pmatrix} = \begin{pmatrix} \sin\theta\cos\varphi \\ \sin\theta\sin\varphi \\ \cos\theta \end{pmatrix}, \quad (4)$$

where θ is the polar angle ($0 \le \theta \le \pi$) and φ is the azimuthal angle ($0 \le \varphi < 2\pi$).

For Compton scattering, the Compton recoil electron energy ($E_{\rm comp}$) and angular emission direction ($\theta_{\rm comp}$) are calculated using equations (5) and (6), respectively:

$$E_{\rm comp} = \frac{E_{\rm inc}^2\left(1-\cos\theta_{\rm pho}\right)}{mc^2\left\{1+\left[E_{\rm inc}\left(1-\cos\theta_{\rm pho}\right)/mc^2\right]\right\}}, \quad (5)$$

$$\tan\theta_{\rm comp} = \frac{1}{\tan\left(\theta_{\rm pho}/2\right)\left(1+E_{\rm inc}/mc^2\right)}. \quad (6)$$

The angular deflection of the photon, $\theta_{\rm pho}$, is chosen as a random angle in radians, where $0 \le \theta_{\rm pho} < \pi$, m is the rest mass of an electron and c is the speed of light. Following Compton scattering, *RADDOSE-XFEL* stops tracking the photon. For a 10 keV photon, the total (Compton effect + photoelectric) MFPL in pure water is 2.07 mm (compared with 2.13 mm for the photoelectric effect alone, as mentioned earlier), so in 10 µm there is again a <0.5% chance of another interaction. Given also that the Compton effect MFPL is ∼30 times higher than that of the photoelectric effect for a 10 keV photon in pure water, the error resulting from neglecting further interactions is negligible.

2.2. Electron simulations

After a photoelectron, Compton recoil electron or Auger electron (Section 2.3) has been produced, the electron is tracked in the manner depicted in Fig. 2.

Similarly to the photon tracking, the first step in the code is to calculate the MFPL to the next interaction. For the electrons, the interactions have been divided into elastic and inelastic scattering. Elastic scattering involves electrostatic interactions between primary electrons and atomic nuclei that alter the direction of electron propagation, but the total kinetic energy of the electron and of the nucleus is conserved. Inelastic scattering, which is ∼3× more likely than elastic interactions for organic specimens (Henderson, 1995), causes primary electrons to lose energy.

The electron elastic scattering cross sections were calculated using the program *ELSEPA* (Salvat *et al.*, 2005) and tabulated in the range 0.05–300 keV for each element. The inelastic cross sections are calculated using the GOS model, which is employed in the program *PENELOPE* (Salvat *et al.*,

2001). The GOS model requires knowledge of the mean excitation energy, I, which is defined for an element by Fano (1963) as

$$\ln I = \sum_n f_n \ln E_n. \quad (7)$$

Here, f_n is the optical dipole oscillator strength for the nth shell and E_n is the shell excitation energy. The values for experimentally determined mean excitation potentials for each atom were taken from reference values in ICRU report 37 (ICRU, 1984) and multiplied by 1.13 to modify them from being in the gas phase to the liquid/solid phase (ICRU, 1984).

The GOS model provides an accurate description of the average effect of inelastic collisions on the projectile but does not necessarily provide accurate inner-shell ionization cross sections (Bote & Salvat, 2008). Inner-shell ionizations are approximately 100-fold less likely to occur than outer-shell ionizations, but are important since they can be followed by Auger emission. These are therefore calculated by a combination of the PWBA and DWBA, as outlined by Bote *et al.* (2009).

Once the electron inelastic and elastic cross sections for each element have been calculated, the elastic, inelastic and total MFPLs for the sample and surrounding material are calculated as in equation (2). The distance to the next interaction can then be determined according to equation (3). The type of collision (elastic or inelastic) is chosen via the inverse sampling method using the relative probabilities of each collision. The choice of element (or elemental shell in the case of an inelastic collision) is made in a similar manner.

For an elastic interaction, the angular deflection of the primary electron is chosen. Discrete probabilities are obtained from the reference differential cross sections (DCSs) in the *ELSEPA* program and sampled using the inverse transform method. The direction vector of the electron is then updated in the 3D polar coordinate system as in equation (4).

For inelastic interactions, the energy loss and angular deflection of the primary electron are calculated via the same method as used in *PENELOPE* (Salvat *et al.*, 2001). The timestamp of this energy deposition event is calculated using the velocity of the electron and the distance travelled since the last timestamp. Secondary electrons produced by these electrons are not simulated in *RADDOSE-XFEL* since these are nearly always of low energy and would thus only have a negligible impact on the dose.

The primary electron is tracked, with its cross sections and MFPLs being updated after each energy change, until it escapes the crystal and surrounding material that is being simulated, or its energy drops below 50 eV, in which case the remaining energy is considered to be deposited in that voxel.

2.3. Atomic relaxations

If an interaction event occurred in the crystal and an inner-shell electron was released, the atom will then relax. The specific electronic transition must be determined so that the Auger electron or fluorescent photon energies can be defined, it can be determined if there is another vacancy to fill, and the excited state lifetime can be calculated. All electron transition probabilities and the relative probabilities of an Auger electron or fluorescent photon being produced were obtained from the EADL database (Cullen *et al.*, 1991; Cullen, 1992). The specific transition is randomly sampled in the program using the inverse transform method. After an initial relaxation, the atom may remain in an excited state. For example, if an atom has electrons in K, L and M shells, a transition of an electron from an L shell to a vacancy in a K shell will result in an L-shell vacancy that can be filled by an electron in an M shell. Account is taken of these multiple ionizations during relaxation using the same method, described below. In *RADDOSE-XFEL*, fluorescent photons are not tracked and are assumed to escape from the crystal. The error from this is negligible since the probability of fluorescent release is small for low-Z elements and fluorescent photons have a high probability of escape from the microcrystals used at XFELs. Auger electrons are sent out in an initial random direction and therefore need to be given a starting timestamp. The lifetime of an excited state, t, before an Auger electron is released is estimated from the Auger linewidths (Γ), which represent the uncertainty in energy of an Auger electron, using Heisenberg's uncertainty principle (Heisenberg, 1927):

$$t \cong \hbar/\Gamma, \quad (8)$$

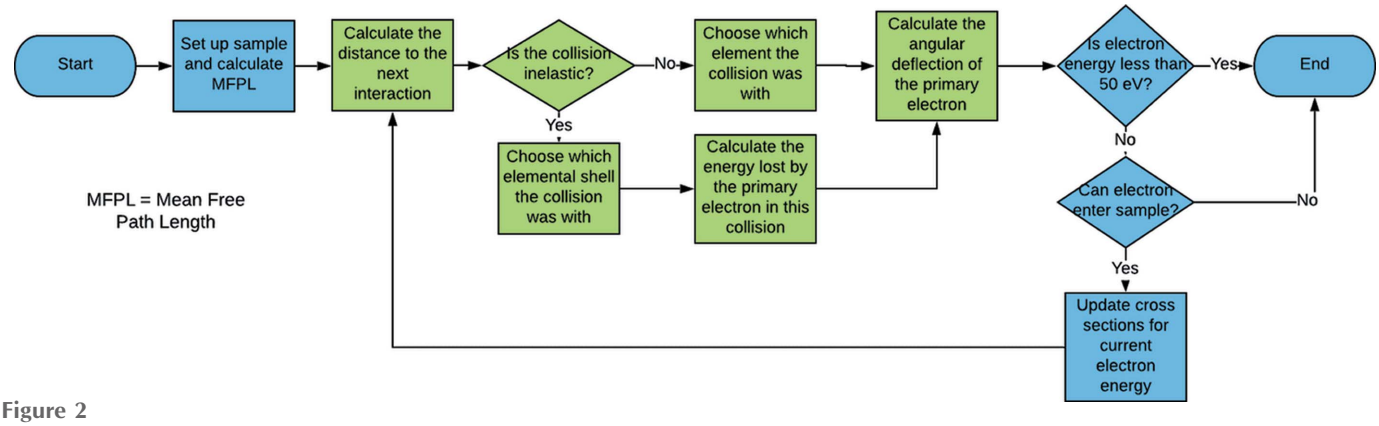

Figure 2
A description of the logical flow of the electron simulations in *RADDOSE-XFEL*. For the processes shown in green, random numbers were used to sample from probability density functions.

where $\hbar$ is Planck's constant divided by 2π. The Auger linewidth for a transition can be estimated by summing the linewidths of all shells involved in the transition (Krause & Oliver, 1979). For example,

$$\Gamma(KL1L2) = \Gamma(K) + \Gamma(L1) + \Gamma(L2), \quad (9)$$

where $\Gamma(KL1L2)$ is the lifetime of an Auger transition if an electron from the $L1$ shell filled a vacancy in the K shell and an electron from the $L2$ shell was released as an Auger electron. The linewidths of all atomic shells for all elements were taken from the recommended values tabulated by Campbell & Papp (2001). Using this method, the K-hole lifetime (calculated by averaging the lifetimes of all possible transitions to fill a K hole, weighted by the probability of this transition occurring relative to all possible K-hole transitions) was found to be 10.8 fs for carbon, 7.1 fs for nitrogen, 4.9 fs for oxygen and 0.55 fs for sulfur. These values closely match those previously reported (Neutze *et al.*, 2000; Chapman *et al.*, 2014) with the exception of sulfur, which has a significantly shorter average lifetime than the 1.3 fs quoted by those authors. A lifetime of 1.3 fs corresponds to a linewidth of ∼0.52 eV, which is the linewidth of the K shell alone.

2.4. Time-resolved energy loss

After relaxation, the energy deposited in the sample by the photon or electron interaction is calculated. The energy deposited for an inner-shell ionization is taken as the energy difference between the initial inner-shell electron-binding energy and the energies of all subsequent Auger electrons and fluorescent photons produced by relaxation of the atom, as illustrated in Fig. 3.

Consider the absorption of a photon by an O atom, resulting in the ejection of an electron [Fig. 3(*a*)]. This can be an outer-shell electron (event 2) or an inner-shell electron (event 1, in this case a K-shell electron). It is intuitive to calculate the energy absorbed by the sample in this event as the photon energy minus the photoelectron energy (*i.e.* the shell binding energy), which is correct for event 2. However, the same cannot be said for event 1, as this is not time resolved. It would imply that inner-shell ionizations are instantly more damaging than outer-shell ionizations, which is unlikely to be the case, and neglects the energy that would be absorbed from Auger electrons and fluorescent photons.

Therefore, before calculating the instantaneously deposited energy in a photon absorption (or an electron scattering from an inner-shell atomic electron), *RADDOSE-XFEL* first determines [Fig. 3(*b*)] the relaxation transition that produces an Auger electron [(ii) in Fig. 3(*b*)] or a fluorescent photon [(i) in Fig. 3(*b*)]. The energy deposited in the first collision is then taken as the energy difference between the initial inner-shell electron binding energy and the energy of the Auger electron (or the fluorescent photon). If there are multiple relaxations, the same principle is applied, and the energy absorbed from the initial ionizing interaction is the initial shell binding energy minus the energy of all Auger electrons and fluorescent photons released.

It is known that approximately 20 eV of energy is absorbed per ionization caused by electrons (Henderson, 1995), and thus for the dose to be proportional to the number of ionizations and the damage, we would expect the dose calculated by *RADDOSE-XFEL* to be similar to this value. For O, the K-shell binding energy is 537 eV and the energy of relaxation products is 523 eV for photons and ranges from 479 eV ($KL1L1$) to 509 eV ($KL3L3$) for Auger transitions. This corresponds to 14 eV for an ionization that results in fluorescence and 14–29 eV per ionization for Auger transitions (Auger decay results in a doubly ionized atom). For carbon this is 9 eV for an ionization that results in fluorescence and 9–18 eV per ionization for Auger transitions. Thus *RADDOSE-XFEL* is in agreement with the accepted values.

2.5. Energy processing

After all photons and subsequent electrons have been simulated, the energy deposited in each voxel before all photons have left it is calculated. The cut-off time C_n for a voxel n is given by equation (10):

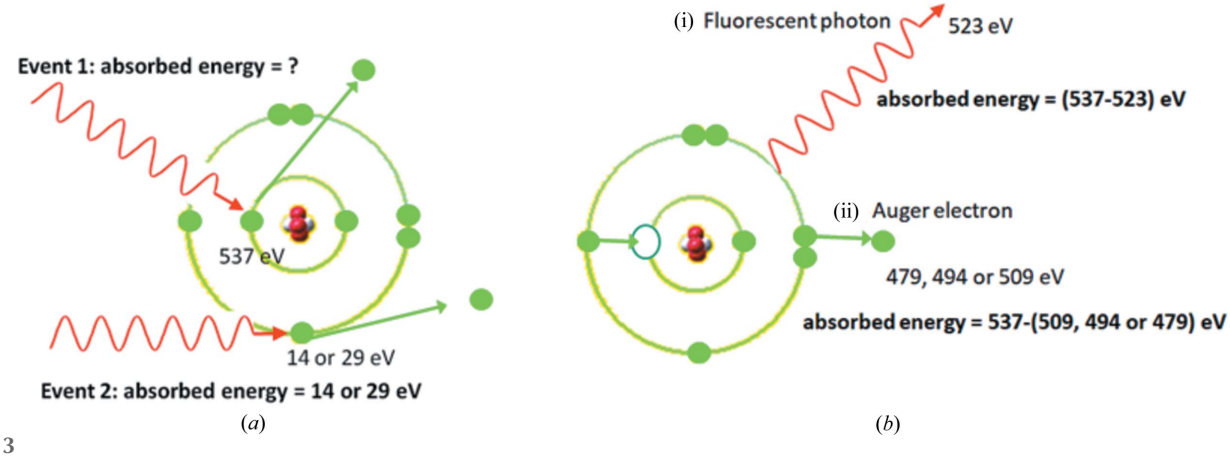

Figure 3
Diagram illustrating how the time-resolved dose is calculated in *RADDOSE-XFEL*. (*a*) Absorption of a photon by an O atom, resulting in the ejection of an electron from an outer-shell electron (event 2) or an inner-shell electron (event 1, in this case a K-shell electron). (*b*) The relaxation transition that produces (i) a fluorescent photon or (ii) an Auger electron.

$$C_n = L + d_n/c. \tag{10}$$

where L is the pulse length, d_n is the depth of the back edge of the voxel and c is the speed of light. The energy deposited in each voxel before time C_n is then multiplied by the factor H:

$$H = \frac{\text{total photons}}{\text{simulated photons}},$$
$$\text{total photons} = \frac{\text{pulse energy}}{\text{mean photon energy}}. \tag{11}$$

3. Program inputs

The input shares many of the same parameters as required for *RADDOSE-3D* (Zeldin, Gerstel & Garman, 2013): a sample input file is shown in Fig. 4. In the `Crystal` block, the user specifies the subprogram as `XFEL` to direct the program to *RADDOSE-XFEL* instead of to the standard *RADDOSE-3D*. The user inputs the number of photons to be simulated (more photons will increase accuracy but the program will take longer to run) and the number of times the program is to be run. It is recommended to run the program more than once to ensure that results are consistent owing to the nature of Monte Carlo simulations. As well as defining the crystal size and composition in the same manner as for *RADDOSE-3D*, the user has the option to define the composition of the surrounding material. As for *RADDOSE-3D*, the user also chooses the number of pixels per micrometre for the crystal, and for *RADDOSE-XFEL* dividing the sample volume into a total of ∼1000 pixels is recommended.

Table 1
Explanation of the metrics output by *RADDOSE-XFEL*.

Output metric	Description
Average dose whole crystal (ADWC)	The average dose across all voxels in the crystal.
Average dose exposed region (ADER)	The average dose across all voxels that fall within the beam area, which is necessary for beams that are smaller than the crystals.
RADDOSE-3D style ADWC	The dose calculated by assuming that all energy from the photoelectric and Compton effects remains in the sample. The average dose across all voxels in the crystal is then output.
RADDOSE-3D style ADER	The dose calculated by assuming that all energy from the photoelectric and Compton effects remains in the sample. The average dose across all voxels that fall within the beam area is then output.
Average ionization per atom	The average number of ionizations per atom in the crystal.
Average ionization per non-hydrogen atom	The average number of ionizations per non-hydrogen atom in the crystal.
Average ionization per atom element	The average number of ionizations per atom in the crystal for each specific element.

In the `Beam` block, the user defines the intensity profile of the beam as top-hat or Gaussian, as in *RADDOSE-3D*. Instead of inputting a flux, the user inputs the pulse energy of the beam. If appropriate, a pink beam can be specified with a Gaussian distribution of photon energies, and an energy FWHM can be input, as discussed above. The user can also define rectangular or circular collimation if any is present.

```
##########################################################################################################################################################################
#                                                                                Crystal Block                                                                           #
##########################################################################################################################################################################
Crystal

Type Cuboid            #Crystal shape can be Cuboid or Spherical
Dimensions 1 1 1       # Dimensions of the crystal in X,Y,Z in µm. Z is the beam axis, Y the rotation axis and X completes the right handed set (vertical if starting face-on).
PixelsPerMicron 10     # This defines the coarseness of the simulation (i.e. how many voxels the crystal is divided into.)

AbsCoefCalc  RD3D      # Absorption Coefficients calculated using RADDOSE-3D (Zeldin et al. 2013).

SUBPROGRAM XFEL        # Selects the RADDOSE-XFEL sub-program
Runs 3                 # Number of RADDOSE-XFEL runs
SIMPHOTONS 1000000     # Number of photons to simulate

UnitCell   78.02  78.02  78.02 90 90 90     # unit cell size: a, b, c with alpha, beta and gamma angles default to 90°
NumMonomers  24                            # number of monomers in unit cell
NumResidues  51                            # number of residues per monomer
ProteinHeavyAtoms  Zn 0.333 S 6            # heavy atoms added to protein part of the monomer, i.e. S, coordinated metals, Se in Se-Met
SolventHeavyConc P 425                     # concentration of elements in the solvent in mmol/l. Oxygen and lighter elements should not be specified
SolventFraction 0.64                       # fraction of the unit cell occupied by solvent

CALCSURROUNDING TRUE          # Whether or not to place a surrounding material around the crystal
SURROUNDINGHEAVYCONC Na 100   #Concentration of heavy atoms in the surrounding material
#DENSITYBASED TRUE            # If true specify surrounding material by elemental composition and density
#SURROUNDINGLELEMENTS C 1     #Specify elements in surrounding material if densitybased = true
#SURROUNDINGDENSITY 1         #Specify density of surrounding material if densitybased = true

##########################################################################################################################################################################
#                                                                                 Beam Block                                                                             #
##########################################################################################################################################################################
Beam

Type Gaussian                  # beam profile can be Gaussian or TopHat
FWHM 1 1                       # in µm, horizontal by vertical full width half maximum for a Gaussian beam
Energy 10                      # Average Photon energy in keV
PulseEnergy 1                  # Energy of the pulse in mJ
EnergyFWHM 0.5                 # Full width half maximum of the energy if pink beam is used
Collimation Rectangular 1 1    # Horizontal/Vertical collimation of the beam

##########################################################################################################################################################################
#                                                                                 Wedge Block                                                                            #
##########################################################################################################################################################################
Wedge 0 0

ExposureTime 30    # Total pulse length in femtoseconds
```

Figure 4
An example of a *RADDOSE-XFEL* input file for insulin crystals.

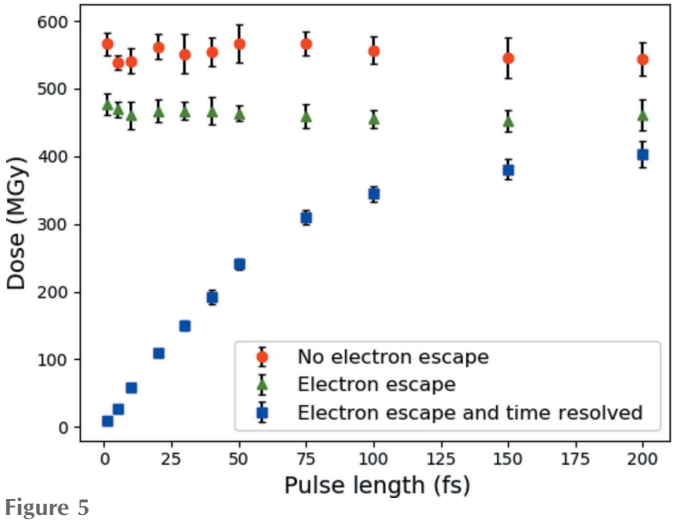

Figure 5
Plot demonstrating how the dose changes with pulse length for lysozyme crystals where the X-ray beam is the same size as the crystal and the number of photons per pulse is kept constant. The red circles are the '*RADDOSE-3D* style' dose with no photoelectron escape, which is how dose has previously been calculated for XFEL experiments. The green triangles are calculated using *RADDOSE-XFEL*, which includes photoelectron escape and entry, without cutting off the simulation at the end of the pulse. The blue squares are calculated using *RADDOSE-XFEL* when the simulation is stopped after the end of the pulse. Error bars are 95% confidence limits for $n = 6$, with 1 000 000 photons simulated for each of six runs.

In the wedge block, the user only needs to specify the pulse length in femtoseconds.

4. Program outputs

The metrics output by *RADDOSE-XFEL* are fully described in Table 1. The final dose of a voxel, D_n, is calculated in *RADDOSE-XFEL* using the following equation:

$$D_n = J_n/V_n\rho, \tag{12}$$

where J_n is the energy deposited in voxel n, V_n is the voxel volume and ρ is the sample density.

RADDOSE-XFEL outputs two dose metrics, the average dose across all voxels in the crystal (average dose whole crystal, ADWC) and the average dose across all voxels that fall within the beam area (average dose exposed region, ADER), which is necessary for beams that are smaller than the crystals.

RADDOSE-XFEL also calculates a '*RADDOSE-3D* style' dose, where all energy from the photoelectric and Compton effects remains in the sample. This dose value is routinely compared with the dose calculated by *RADDOSE-3D*. If there is a significant difference, a warning is displayed and the user is advised to increase the number of photons that are being simulated.

The average diffraction weighted dose (DWD) (Zeldin, Brockhauser *et al.*, 2013) output by *RADDOSE-3D* is not output by *RADDOSE-XFEL*. To be reliably calculated, DWD requires several orders of magnitude more simulated photons than do the other dose metrics. Hence it is recommended that when quoting the absorbed dose for XFEL experiments, researchers should always use the ADER.

5. Changes in dose values compared with *RADDOSE-3D* output

As a result of including escape of electrons from the crystal and neglecting the energy deposited after the end of the pulse, *RADDOSE-XFEL* produces much lower dose estimates than those calculated by previous methods. To illustrate this, the doses for lysozyme crystals were calculated with different pulse lengths (Fig. 5). Fig. 5 shows a reduction in dose when electron tracks are simulated (green triangles) due to the net

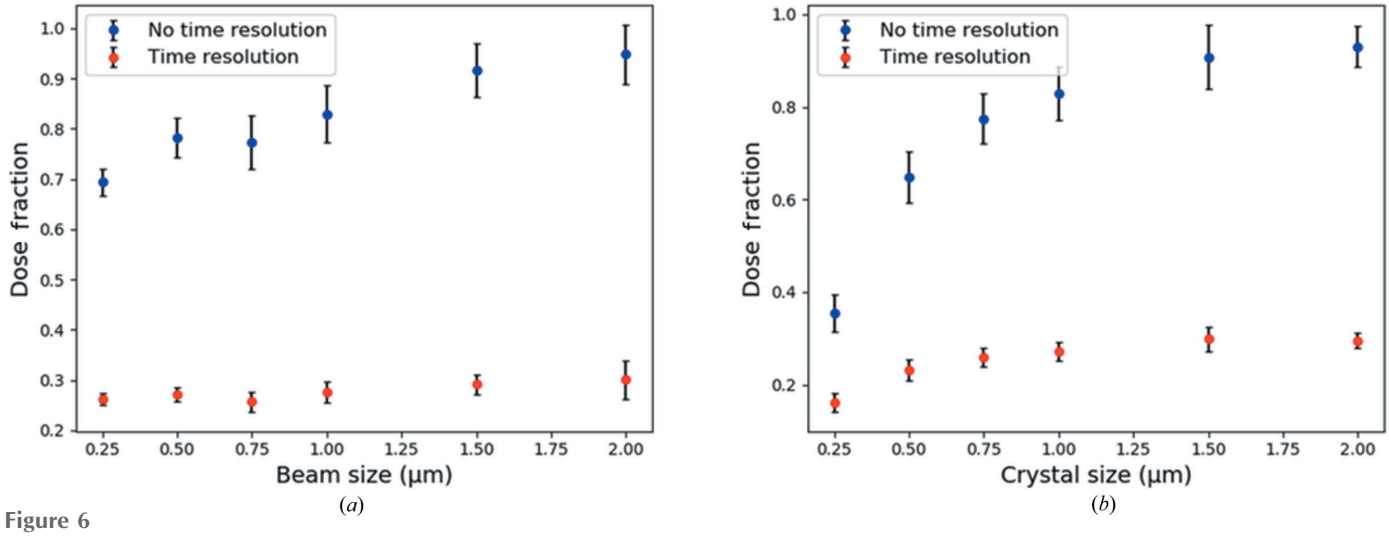

Figure 6
Plot demonstrating how the dose changes with (*a*) beam size and (*b*) crystal size for lysozyme crystals. In (*a*) the crystal is 1 × 1 × 1 μm in size and in (*b*) the beam size is matched to the crystal size. The blue circles correspond to the dose calculated by *RADDOSE-XFEL* when all the deposited energy (irrespective of timestamp) is included in the dose, and the red circles are the *RADDOSE-XFEL* ADER. The dose fractions are these doses divided by the *RADDOSE-3D* style ADER. Error bars are 95% confidence limits for $n = 6$, with 500 000 photons simulated for each of six runs.

escape of electrons from the crystal. When only the dose during the length of the pulse is considered, it is further reduced, with shorter pulses resulting in lower doses (there is an 84% reduction in dose for a 1 fs pulse compared with the *RADDOSE-3D* computed dose). Hence, XFEL doses calculated using *RADDOSE-3D* are too high, since the correct physical effects are not being taken into account.

The difference between the doses calculated by *RADDOSE-3D* and *RADDOSE-XFEL* increases not only as the pulse length shortens but also as crystal size and beam size reduce, owing to the greater net escape of electrons from the crystal (Fig. 6).

6. Example of a *RADDOSE-XFEL* run

Doses calculated by Boutet *et al.* (2012) for data collection from hen egg-white lysozyme crystals at an XFEL (LCLS) were recalculated using *RADDOSE-XFEL*. In the Boutet *et al.* study, data were collected at 9.4 keV using a 5 fs pulse with pulse energy 53 µJ, and a 40 fs pulse with pulse energy 600 µJ. The doses were reported to be ∼2.9 MGy per crystal for the 5 fs pulse and ∼33 MGy per crystal for the 40 fs pulse. The full *RADDOSE-XFEL* input for the 40 fs pulse is shown in Fig. 7. The input file was run three times with the crystal in three orientations and the results averaged. The simulation was therefore run 18 times with 250 000 photons per run. Each run took 150 ± 13 s to complete (performed using a 3.70 GHz Intel i3-4170 processor and 8.0 GB of RAM). The results are shown in Table 2.

The *RADDOSE-3D* output ADWC doses presented in Table 2 are slightly higher than those reported by Boutet *et al.* (2012), which may be a result of slight differences in the buffer composition included in the calculation.

Overall, there is an approximately 13-fold reduction in dose for a 5 fs pulse when *RADDOSE-XFEL* is used compared with the standard *RADDOSE-3D* result and an approximately 2.3-fold reduction for the 40 fs pulse. As evidenced by the simulations shown in Fig. 5, this reduction is partly a result of photoelectrons escaping the sample, but the major effect is from the pulses finishing before the majority of photoelectron damage has occurred.

Table 2
Results from running *RADDOSE-XFEL* on the input described in Fig. 7.

The input file was run three times with the crystal in three orientations and the results averaged. The simulation was therefore run 18 times with 250 000 photons per run.

Pulse length (fs)	Boutet *et al.* (2012) reported dose (MGy)	*RADDOSE-3D* style ADWC (MGy)	*RADDOSE-XFEL* ADWC (MGy)
5	∼2.9	3.4 ± 0.2	0.26 ± 0.02
40	∼33	39.2 ± 2.2	17.1 ± 1.0

7. Discussion

The need for using *RADDOSE-XFEL* instead of *RADDOSE-3D* or other methods to calculate doses at XFELs has been demonstrated (Figs. 5 and 6, and Table 2). The difference between *RADDOSE-3D* and *RADDOSE-XFEL* increases as pulse length decreases and also, to a lesser extent, as the crystal size and beam size are reduced.

Since dose accounts for differences in experimental parameters such as photon energy and sample composition, it can be used as a metric to compare the extent of radiation damage between different experiments. Dose is a well established metric for tracking the extent of radiation damage at conventional X-ray sources and, although there have only been a handful of radiation damage experiments conducted at XFELs so far (Nass, 2019), estimated doses could be used similarly at XFELs. *RADDOSE-3D* and its predecessors have been used to estimate doses for radiation damage studies at

```
##############################################################################################################################################################
#                                                                    Crystal Block                                                                           #
##############################################################################################################################################################
Crystal

Type Cuboid            # Crystal shape can be Cuboid or Spherical
Dimensions 1 1 3       # Dimensions of the crystal in X,Y,Z in µm. Z is the beam axis, Y the rotation axis and X completes the right handed set (vertical if starting face-on).
PixelsPerMicron 8      # This defines the coarseness of the simulation (i.e. how many voxels the crystal is divided into.)

AbsCoefCalc  Exp       # Absorption Coefficients calculated using RADDOSE-3D (Zeldin et al. 2013).


SUBPROGRAM XFEL        # Selects the RADDOSE-XFEL sub-program
Runs 6                 # Number of RADDOSE-XFEL runs
SIMPHOTONS 250000      # Number of photons to simulate

PDB 2VB1
SolventHeavyConc Na 2700 Cl 1700      # concentration of elements in the solvent in mmol/l. Oxygen and lighter elements should not be specified

CALCSURROUNDING TRUE    # Whether or not to place a surrounding material around the crystal

##############################################################################################################################################################
#                                                                    Beam Block                                                                              #
##############################################################################################################################################################
Beam

Type TopHat                         # beam profile can be Gaussian or TopHat

Energy 9.4                          # Average Photon energy in keV
PulseEnergy 0.6                     # Energy of the pulse in mJ
Collimation Rectangular 3.16 3.16   # Horizontal/Vertical collimation of the beam

##############################################################################################################################################################
#                                                                    Wedge Block                                                                             #
##############################################################################################################################################################
Wedge 0 0

ExposureTime 40    # Total pulse length in femtoseconds
```

Figure 7
RADDOSE-XFEL input file for the 40 fs pulse from the work of Boutet *et al.* (2012).

XFELs in the past (Lomb *et al.*, 2011; Nass *et al.*, 2015), but these values are overestimates because they do not take into account photoelectron escape and are not time resolved on the femtosecond timescale. *RADDOSE-XFEL* will provide more accurate dose estimates for studies similar to these.

RADDOSE-XFEL may also help facilitate the elucidation of a dose limit at which radiation damage would be predicted to manifest in the diffraction patterns. The software could then be run by a user in a few minutes prior to data collection, and the experimental parameters could be adjusted to ensure that the dose remains below this limit. As an estimate, a limit of an average of one ionization per atom has been suggested, since up to this point most scattering during the pulse will be from pristine atoms (Chapman *et al.*, 2014) that do not have their scattering power reduced by ionization (Caleman *et al.*, 2011). The corresponding dose was calculated to be 400 MGy (Chapman *et al.*, 2014), and *RADDOSE-XFEL* simulations approximately agree with this estimate (Fig. S1). Heavy elements will reach a one ionization per atom limit faster than average atoms, and specific damage to these may therefore be seen at lower doses. The *RADDOSE-XFEL* output of ionizations per atom for each element may in the future enable an indication to be obtained as to when specific damage may occur.

However, the dose calculation only accounts for ionizing damage (which alters the atomic scattering factors), and molecular motion would also need to be considered in order to predict when global damage will manifest. It is clear that some molecular motion is being outrun by XFEL pulses since the doses at which damage is observed are still much higher at XFEL sources than in cryo-cooled proteins at synchrotrons (Nass *et al.*, 2015), but XFEL pulses do not necessarily entirely outrun atomic motion. A similar atomic displacement term to that employed by Barty *et al.* (2012), which was used to determine the onset of Bragg termination (crystal disorder ending diffraction), would need to be incorporated into *RADDOSE-XFEL* to inform users of the extent to which different resolution shells have been affected by atomic displacements. The program could then inform the user when to stop collecting data because crystal disorder and ionizing damage have occurred.

Improvements in the accuracy of the dose and number of ionizations calculated by *RADDOSE-XFEL* may also be required to better predict, prior to data collection, what level of damage will manifest in diffraction patterns. Firstly, ionization of the atoms in the sample will alter their cross sections to photons and electrons (Hau-Riege, 2007; Caleman *et al.*, 2011). Ejection of a *K*-shell photoelectron will significantly reduce the photoelectric absorption cross section of an atom until the atom relaxes and refills the *K* shell (Neutze *et al.*, 2000; Young *et al.*, 2010). This 'radiation hardening' is likely to reduce the number of ionizations per atom and thus also somewhat lower the dose. Secondly, the number of ionizations will also be affected by the lack of hole scattering and electron–hole recombination. In hole scattering, impact ionization from the valence band in semiconductors and insulators releases a pair of carriers in the form of an electron and a hole. Holes can move inside the valence band and they themselves can cause further impact ionizations through hole scattering. In diamond, neglecting hole scattering can reduce the number of ionizations by as much as a factor of two (Ziaja *et al.*, 2005; Gabrysch *et al.*, 2008). Electron–hole recombinations would have the opposite effect and reduce the number of ionizations, hence causing charge reduction.

Comparisons were made between molecular dynamics (MD) using electron impact ionization cross sections from neutral crystals and the plasma dynamics code *CRETIN* (Scott & Mayle, 1994; Scott, 2001), which accounts for changes in cross section due to ionizations and includes electron–hole recombination and hole scattering (Caleman *et al.*, 2011). In the plasma model, there are more ionizations per atom in the beginning part of the pulse than are simulated in MD, because only in the plasma model is account taken of hole scattering. As the pulse length increases and the sample is damaged, the neutral crystal approach and lack of electron–hole recombination causes the MD simulations to overestimate the number of ionizations per atom, and *RADDOSE-XFEL* will do the same.

As well as lack of radiation hardening, the neutral crystal approach also precludes *RADDOSE-XFEL* from simulating the effect of charging both on the dose and on the number of ionizations per atom. As electrons begin to escape from the crystal volume, there will be a net build-up of positive charge in the sample that will increase the rate of entry of photoelectrons from the surroundings, and this will decrease the rate of photoelectron escape. Neglecting this charging will thus be likely to reduce the calculated dose and the number of ionizations per atom. The trapped electrons will also significantly impact the damage kinetics, since the trapped electrons cause secondary collisional ionizations (Hau-Riege *et al.*, 2004; Hau-Riege, 2012). We plan to incorporate an option to include radiation hardening and charge in *RADDOSE-XFEL* simulations in the future, although these will increase the runtime of the program.

8. Summary

RADDOSE-XFEL is an extension to the free and open-source software *RADDOSE-3D* to allow the rapid estimation of the absorbed dose of samples at XFEL sources. Use of this software will aid radiation damage studies at XFELs and may facilitate the identification of a damage limit. The code can be found at https://github.com/GarmanGroup/RADDOSE-3D/releases.

9. Related literature

The following additional literature is cited in the supporting information: Berger *et al.* (2005, 2016), Bethe (1930, 1932), Cooper & Zare (1968), Koch *et al.* (1983), McMaster *et al.* (1969) and Rybicki & Lightman (1979).

Acknowledgements

We are grateful to Karol Nass and Jeney Wierman for testing the program for their experimental XFEL conditions, to

Sébastien Boutet for providing us with LCLS energy profiles, and to Ian Carmichael for useful discussions and also for comments on the manuscript.

Funding information

We thank the Laidlaw Scholars Programme (JLD) and the EPSRC Vacation Placement Programme (PTNM) for funding this work.

References

Auger, P. (1925). *J. Phys. Radium*, **6**, 205–208.
Barty, A., Caleman, C., Aquila, A., Timneanu, N., Lomb, L., White, T. A., Andreasson, J., Arnlund, D., Bajt, S., Barends, T. R. M., Barthelmess, M., Bogan, M. J., Bostedt, C., Bozek, J. D., Coffee, R., Coppola, N., Davidsson, J., DePonte, D. P., Doak, R. B., Ekeberg, T., Elser, V., Epp, S. W., Erk, B., Fleckenstein, H., Foucar, L., Fromme, P., Graafsma, H., Gumprecht, L., Hajdu, J., Hampton, C. Y., Hartmann, R., Hartmann, A., Hauser, G., Hirsemann, H., Holl, P., Hunter, M. S., Johansson, L., Kassemeyer, S., Kimmel, N., Kirian, R. A., Liang, M., Maia, F. R. N. C., Malmerberg, E., Marchesini, S., Martin, A. V., Nass, K., Neutze, R., Reich, C., Rolles, D., Rudek, B., Rudenko, A., Scott, H., Schlichting, I., Schulz, J., Seibert, M. M., Shoeman, R. L., Sierra, R. G., Soltau, H., Spence, J. C. H., Stellato, F., Stern, S., Strüder, L., Ullrich, J., Wang, X., Weidenspointner, G., Weierstall, U., Wunderer, C. B. & Chapman, H. N. (2012). *Nat. Photon.* **6**, 35–40.
Berendsen, H. J. C., van der Spoel, D. & van Drunen, R. (1995). *Comput. Phys. Commun.* **91**, 43–56.
Berger, M. J., Coursey, J. S., Zucker, M. A. & Chang, J. (2005). NIST Standard Reference Database. National Institute of Standards and Technology, Gaithersburg, MD, USA.
Berger, M. J., Hubbell, J. H., Seltzer, S. M., Chang, J., Coursey, J. S., Sukumar, R., Zucker, D. S. & Olsen, K. (2010). *XCOM: Photon Cross Sections Database*, https://www.nist.gov/pml/xcom-photon-cross-sections-database.
Berger, M. J., Inokuti, M., Anderson, H. H., Bichsel, H., Dennis, J. A., Powers, D., Seltzer, S. M. & Turner, J. E (2016). *J. Int. Comm. Radiat. Units Meas.* **os19**, https://doi.org/10.1093/jicru/os19.2.Report37.
Bethe, H. A. (1930). *Ann. Phys.* **397**, 325–400.
Bethe, H. A. (1932). *Z. Phys.* **76**, 293–299.
Blake, C. C. F. & Phillips, D. C. (1962). *Biological Effects of Ionizing Radiation at the Molecular Level*, International Atomic Energy Agency Proceedings Series, pp. 183–191. Vienna: IAEA.
Bote, D. & Salvat, F. (2008). *Phys. Rev. A*, **77**, 042701.
Bote, D., Salvat, F., Jablonski, A. & Powell, C. J. (2009). *At. Data Nucl. Data Tables*, **95**, 871–909.
Boutet, S., Lomb, L., Williams, G. J., Barends, T. R. M., Aquila, A., Doak, R. B., Weierstall, U., DePonte, D. P., Steinbrener, J., Shoeman, R. L., Messerschmidt, M., Barty, A., White, T. A., Kassemeyer, S., Kirian, R. A., Seibert, M. M., Montanez, P. A., Kenney, C., Herbst, R., Hart, P., Pines, J., Haller, G., Gruner, S. M., Philipp, H. T., Tate, M. W., Hromalik, M., Koerner, L. J., van Bakel, N., Morse, J., Ghonsalves, W., Arnlund, D., Bogan, M. J., Caleman, C., Fromme, R., Hampton, C. Y., Hunter, M. S., Johansson, L. C., Katona, G., Kupitz, C., Liang, M., Martin, A. V., Nass, K., Redecke, L., Stellato, F., Timneanu, N., Wang, D., Zatsepin, N. A., Schafer, D., Defever, J., Neutze, R., Fromme, P., Spence, J. C. H., Chapman, H. N. & Schlichting, I. (2012). *Science*, **337**, 362–364.
Bury, C. S., Brooks-Bartlett, J. C., Walsh, S. P. & Garman, E. F. (2018). *Protein Sci.* **27**, 217–228.
Caleman, C., Bergh, M., Scott, H. A., Spence, J. C. H., Chapman, H. N. & Tîmneanu, N. (2011). *J. Mol. Opt.* **58**, 1486–1497.
Campbell, J. L. & Papp, T. (2001). *At. Data Nucl. Data Tables*, **77**, 1–56.
Chapman, H. N., Caleman, C. & Timneanu, N. (2014). *Philos. Trans. R. Soc. London B Biol. Sci.* **369**, 20130313.
Chapman, H. N., Fromme, P., Barty, A., White, T. A., Kirian, R. A., Aquila, A., Hunter, M. S., Schulz, J., DePonte, D. P., Weierstall, U., Doak, R. B., Maia, F. R. N. C., Martin, A. V., Schlichting, I., Lomb, L., Coppola, N., Shoeman, R. L., Epp, S. W., Hartmann, R., Rolles, D., Rudenko, A., Foucar, L., Kimmel, N., Weidenspointner, G., Holl, P., Liang, M., Barthelmess, M., Caleman, C., Boutet, S., Bogan, M. J., Krzywinski, J., Bostedt, C., Bajt, S., Gumprecht, L., Rudek, B., Erk, B., Schmidt, C., Hömke, A., Reich, C., Pietschner, D., Strüder, L., Hauser, G., Gorke, H., Ullrich, J., Herrmann, S., Schaller, G., Schopper, F., Soltau, H., Kühnel, K., Messerschmidt, M., Bozek, J. D., Hau-Riege, S. P., Frank, M., Hampton, C. Y., Sierra, R. G., Starodub, D., Williams, G. J., Hajdu, J., Timneanu, N., Seibert, M. M., Andreasson, J., Rocker, A., Jönsson, O., Svenda, M., Stern, S., Nass, K., Andritschke, R., Schröter, C., Krasniqi, F., Bott, M., Schmidt, K. E., Wang, X., Grotjohann, I., Holton, J. M., Barends, T. R. M., Neutze, R., Marchesini, S., Fromme, R., Schorb, S., Rupp, D., Adolph, M., Gorkhover, T., Andersson, I., Hirsemann, H., Potdevin, G., Graafsma, H., Nilsson, B. & Spence, J. C. H. (2011). *Nature*, **470**, 73–77.
Cooper, J. & Zare, R. N. (1968). *J. Chem. Phys.* **48**, 942.
Cullen, D. E. (1992). *RELAX: a Code Designed to Calculate X-ray and Electron Emission Spectra as Singly Charged Atoms Relax Back to Neutrality*. Lawrence Livermore National Laboratory, Livermore, CA, USA.
Cullen, D. E., Perkins, S. T., Chen, M. H. & Hubbell, J. H. (1991). *Tables and Graphs of Atomic Subshell and Relaxation Data Derived from the LLNL Evaluated Atomic Data Library (EADL), Z = 1–100.* Lawrence Livermore National Laboratory, Livermore, CA, USA.
Dickerson, J. L. & Garman, E. F. (2019). *J. Synchrotron Rad.* **26**, 922–930.
Ditmire, T. (2016). *High Intensity Femtosecond XUV Pulse Interactions with Atomic Clusters: Final Report*. The University of Texas at Austin, Austin, TX, USA.
Einstein, A. (1905). *Ann. Phys.* **322**, 132–148.
Fano, U. (1963). *Annu. Rev. Nucl. Sci.* **13**, 1–66.
Fourme, R., Honkimäki, V., Girard, E., Medjoubi, K., Dhaussy, A.-C. & Kahn, R. (2012). *J. Appl. Cryst.* **45**, 652–661.
Gabrysch, M., Marklund, E., Hajdu, J., Twitchen, D. J., Rudati, J., Lindenberg, A. M., Caleman, C., Falcone, R. W., Tschentscher, T., Moffat, K., Bucksbaum, P. H., Als-Nielsen, J., Nelson, A. J., Siddons, D. P., Emma, P. J., Krejcik, P., Schlarb, H., Arthur, J., Brennan, S., Hastings, J. & Isberg, J. (2008). *J. Appl. Phys.* **103**, 064909.
Galli, L., Son, S. K., Klinge, M., Bajt, S., Barty, A., Bean, R., Betzel, C., Beyerlein, K. R., Caleman, C., Doak, R. B., Duszenko, M., Fleckenstein, H., Gati, C., Hunt, B., Kirian, R. A., Liang, M., Nanao, M. H., Nass, K., Oberthür, D., Redecke, L., Shoeman, R., Stellato, F., Yoon, C. H., White, T. A., Yefanov, O., Spence, J. & Chapman, H. N. (2015). *Struct. Dyn.* **2**, 1–8.
Hau-Riege, S. P. (2007). *Phys. Rev. A*, **76**, 042511.
Hau-Riege, S. P. (2012). *Phys. Rev. Lett.* **108**, 238101.
Hau-Riege, S. P., London, R. A., Huldt, G. & Chapman, H. N. (2005). *Phys. Rev. E*, **71**, 1–6.
Hau-Riege, S. P., London, R. A. & Szoke, A. (2004). *Phys. Rev. E*, **69**, 12.
Heisenberg, W. (1927). *Z. Phys.* **43**, 172–198.
Henderson, R. (1995). *Q. Rev. Biophys.* **28**, 171–193.
ICRU (1984). *Stopping Powers for Electrons and Positrons*. International Commission on Radiation Units and Measurements, Bethesda, MD, USA.
Joy, D. C. (1995). *Monte Carlo Modeling for Electron Microscopy and Microanalysis*. New York: Oxford University Press.
Koch, E. E., Eastman, D. E. & Farges, Y. (1983). *Handbook of Synchrotron Radiation*, pp. 1–63. Amsterdam: North-Holland Publishing Company.
Krause, M. O. (1979). *J. Phys. Chem. Ref. Data*, **8**, 307–327.

Krause, M. O. & Oliver, J. H. (1979). *J. Phys. Chem. Ref. Data*, **8**, 329–338.
Lomb, L., Barends, T. R. M., Kassemeyer, S., Aquila, A., Epp, S. W., Erk, B., Foucar, L., Hartmann, R., Rudek, B., Rolles, D., Rudenko, A., Shoeman, R. L., Andreasson, J., Bajt, S., Barthelmess, M., Barty, A., Bogan, M. J., Bostedt, C., Bozek, J. D., Caleman, C., Coffee, R., Coppola, N., Deponte, D. P., Doak, R. B., Ekeberg, T., Fleckenstein, H., Fromme, P., Gebhardt, M., Graafsma, H., Gumprecht, L., Hampton, C. Y., Hartmann, A., Hauser, G., Hirsemann, H., Holl, P., Holton, J. M., Hunter, M. S., Kabsch, W., Kimmel, N., Kirian, R. A., Liang, M., Maia, F. R. N. C., Meinhart, A., Marchesini, S., Martin, A. V., Nass, K., Reich, C., Schulz, J., Seibert, M. M., Sierra, R., Soltau, H., Spence, J. C. H., Steinbrener, J., Stellato, F., Stern, S., Timneanu, N., Wang, X., Weidenspointner, G., Weierstall, U., White, T. A., Wunderer, C., Chapman, H. N., Ullrich, J., Strüder, L. & Schlichting, I. (2011). *Phys. Rev. B*, **84**, 1–6.
Marman, H., Darmanin, C. & Abbey, B. (2018). *Crystals*, **8**, 267.
McMaster, W. H., Del Grande, N. K., Mallett, J. H. & Hubbell, J. H. (1969). Report UCRL-50174. Lawrence Livermore National Laboratory, Livermore, CA, USA.
Meitner, L. (1922). *Z. Phys.* **9**, 131–144.
Moseley, H. G. J. (1913). *London Edinb. Dubl. Philos. Mag. J. Sci.* **26**, 1024–1034.
Murray, J. W., Garman, E. F. & Ravelli, R. B. G. (2004). *J. Appl. Cryst.* **37**, 513–522.
Nass, K. (2019). *Acta Cryst.* D**75**, 211–218.
Nass, K., Foucar, L., Barends, T. R. M., Hartmann, E., Botha, S., Shoeman, R. L., Doak, R. B., Alonso-Mori, R., Aquila, A., Bajt, S., Barty, A., Bean, R., Beyerlein, K. R., Bublitz, M., Drachmann, N., Gregersen, J., Jönsson, H. O., Kabsch, W., Kassemeyer, S., Koglin, J. E., Krumrey, M., Mattle, D., Messerschmidt, M., Nissen, P., Reinhard, L., Sitsel, O., Sokaras, D., Williams, G. J., Hau-Riege, S., Timneanu, N., Caleman, C., Chapman, H. N., Boutet, S. & Schlichting, I. (2015). *J. Synchrotron Rad.* **22**, 225–238.
Nave, C. & Garman, E. F. (2005). *J. Synchrotron Rad.* **12**, 257–260.
Nave, C. & Hill, M. A. (2005). *J. Synchrotron Rad.* **12**, 299–303.
Neutze, R., Wouts, R., van der Spoel, D., Weckert, E. & Hajdu, J. (2000). *Nature*, **406**, 752–757.
O'Neill, P., Stevens, D. L. & Garman, E. (2002). *J. Synchrotron Rad.* **9**, 329–332.
Owen, R. L., Rudiño-Piñera, E. & Garman, E. F. (2006). *Proc. Natl Acad. Sci.* **103**, 4912–4917.
Paithankar, K. S., Owen, R. L. & Garman, E. F. (2009). *J. Synchrotron Rad.* **16**, 152–162.
Rybicki, G. B. & Lightman, A. P. (1979). *Radiaitve Processes in Astrophysics*. New York: John Wiley & Sons.
Salvat, F., Fernandez-Varea, J. M., Acosta, E. & Sempau, J. (2001). *PENELOPE – a Code System for Monte Carlo Simulation of Electron and Photon Transport.* Organisation for Economic Co-Operation and Development Nuclear Energy Agency, Paris, France.
Salvat, F., Jablonski, A. & Powell, C. J. (2005). *Comput. Phys. Commun.* **165**, 157–190.
Sanishvili, R., Yoder, D. W., Pothineni, S. B., Rosenbaum, G., Xu, S., Vogt, S., Stepanov, S., Makarov, O. A., Corcoran, S., Benn, R., Nagarajan, V., Smith, J. L. & Fischetti, R. F. (2011). *Proc. Natl Acad. Sci.* **108**, 6127–6132.
Scott, H. A. (2001). *J. Quant. Spectrosc. Radiat. Transfer*, **71**, 689–701.
Scott, H. A. & Mayle, R. W. (1994). *Appl. Phys. B*, **58**, 35–43.
Seibert, M. M., Ekeberg, T., Maia, F. R. N. C., Svenda, M., Andreasson, J., Jönsson, O., Odić, D., Iwan, B., Rocker, A., Westphal, D., Hantke, M., DePonte, D. P., Barty, A., Schulz, J., Gumprecht, L., Coppola, N., Aquila, A., Liang, M., White, T. A., Martin, A., Caleman, C., Stern, S., Abergel, C., Seltzer, V., Claverie, J.-M., Bostedt, C., Bozek, J. D., Boutet, S., Miahnahri, A. A., Messerschmidt, M., Krzywinski, J., Williams, G., Hodgson, K. O., Bogan, M. J., Hampton, C. Y., Sierra, R. G., Starodub, D., Andersson, I., Bajt, S., Barthelmess, M., Spence, J. C. H., Fromme, P., Weierstall, U., Kirian, R., Hunter, M., Doak, R. B., Marchesini, S., Hau-Riege, S. P., Frank, M., Shoeman, R. L., Lomb, L., Epp, S. W., Hartmann, R., Rolles, D., Rudenko, A., Schmidt, C., Foucar, L., Kimmel, N., Holl, P., Rudek, B., Erk, B., Hömke, A., Reich, C., Pietschner, D., Weidenspointner, G., Strüder, L., Hauser, G., Gorke, H., Ullrich, J., Schlichting, I., Herrmann, S., Schaller, G., Schopper, F., Soltau, H., Kühnel, K.-U., Andritschke, R., Schröter, C.-D., Krasniqi, F., Bott, M., Schorb, S., Rupp, D., Adolph, M., Gorkhover, T., Hirsemann, H., Potdevin, G., Graafsma, H., Nilsson, B., Chapman, H. N. & Hajdu, J. (2011). *Nature*, **470**, 78–81.
Son, S. K., Young, L. & Santra, R. (2011). *Phys. Rev. A At. Mol. Opt. Phys.* **83**, 1–11.
Warkentin, M. & Thorne, R. E. (2010). *Acta Cryst.* D**66**, 1092–1100.
Young, L., Kanter, E. P., Krässig, B., Li, Y., March, A. M., Pratt, S. T., Santra, R., Southworth, S. H., Rohringer, N., Dimauro, L. F., Doumy, G., Roedig, C. A., Berrah, N., Fang, L., Hoener, M., Bucksbaum, P. H., Cryan, J. P., Ghimire, S., Glownia, J. M., Reis, D. A., Bozek, J. D., Bostedt, C. & Messerschmidt, M. (2010). *Nature*, **466**, 56–61.
Zeldin, O. B., Brockhauser, S., Bremridge, J., Holton, J. M. & Garman, E. F. (2013). *Proc. Natl Acad. Sci.* **110**, 20551–20556.
Zeldin, O. B., Gerstel, M. & Garman, E. F. (2013). *J. Appl. Cryst.* **46**, 1225–1230.
Ziaja, B., London, R. A. & Hajdu, J. (2005). *J. Appl. Phys.* **97**, 64905.